

Edge transport and turbulence reduction with lithium coated plasma facing components in the National Spherical Torus Experiment^{a)}

J. M. Canik,^{1,b)} R. Maingi,¹ S. Kubota,² Y. Ren,³ R. E. Bell,³ J. D. Callen,⁴ W. Guttenfelder,³ H. W. Kugel,³ B. P. LeBlanc,³ T. H. Osborne,⁵ and V. A. Soukhanovskii⁶

¹Oak Ridge National Laboratory, Oak Ridge, Tennessee 37831, USA

²University of California-Los Angeles, Los Angeles, California 90095, USA

³Princeton Plasma Physics Laboratory, Princeton, New Jersey 08543, USA

⁴University of Wisconsin-Madison, Madison, Wisconsin 53706, USA

⁵General Atomics, San Diego, California 92186, USA

⁶Lawrence Livermore National Laboratory, Livermore, California 94551, USA

(Received 25 February 2011; accepted 28 April 2011; published online 26 May 2011; publisher error corrected 8 June 2011)

The coating of plasma facing components (PFCs) with lithium improves energy confinement and eliminates ELMs in the National Spherical Torus Experiment, the latter due to a relaxation of the density and pressure profiles that reduces the drive for peeling-ballooning modes. 2-D interpretive transport modeling of discharges without and with lithium shows that a reduction in the PFC recycling coefficient from $R \sim 0.98$ to $R \sim 0.90$ is required to match the drop in D_α emission with lithium coatings. A broadening of the edge barrier region showing reduced transport coefficients is observed, with a $\sim 75\%$ drop of the D and χ_e from $0.8 < \psi_N < 0.93$ needed to match the profile relaxation with lithium coatings. Turbulence measurements using an edge reflectometry system as well as high- k microwave scattering show a decrease in density fluctuations with lithium coatings. These transport changes allow the realization of very wide pedestals, with a $\sim 100\%$ width increase relative to the reference discharges. © 2011 American Institute of Physics. [doi:10.1063/1.3592519]

I. INTRODUCTION

Understanding, prediction, and control of the edge pedestal¹ in the H-mode² are a critical area of research for realizing fusion reactors based on the tokamak concept. In order to maximize both energy confinement and global MHD stability, high pressures at the top of the pedestal are desired. However, the onset of peeling-ballooning instabilities³ resulting in edge-localized modes (ELMs) limits the achievable pressure gradient, and therefore, the pedestal-top pressure for a fixed pedestal width. Furthermore, the energy released onto the plasma facing components (PFCs) by ELMs can cause substantial damage to the PFCs, shortening their lifetime.⁴ One mechanism by which these instabilities can be avoided while simultaneously achieving high pedestal-top pressures is by the formation of wide pedestals.

Experiments in the National Spherical Torus Experiment (NSTX) have shown that applying lithium coatings⁵ to the PFCs leads to a favorable modification to the pedestal structure, giving the desired wide pressure pedestal and high edge pressure, while avoiding ELMs.^{6,7} These discharges have improved energy confinement compared to plasmas without lithium coated PFCs.⁸ It has long been observed that the edge conditions of a tokamak, as well as the overall plasma confinement, are affected by wall conditioning.^{9–13} Some of the improvement to performance and discharge reliability allowed by, e.g., low- Z wall coatings can be understood to be due to

the reduction of high- Z impurities and control of particle recycling that these conditioning techniques afford. However, wall conditioning techniques have also often allowed access to improved confinement regimes, such as the TFTR supershot¹⁴ and the VH-mode at DIII-D.¹⁵ While some mechanisms by which conditioning can affect confinement have been identified, such as through convective energy flux or by changes in charge-exchange momentum losses impacting radial electric field and turbulent transport,¹⁶ the overall interplay between edge conditions and global confinement remains poorly understood. This paper presents modeling of NSTX discharges without and with lithium coatings, in order to further the understanding of how lithium modifies the edge plasma transport, resulting in wider pedestals and the elimination of ELMs.

The two discharges that are the focus of this work have been analyzed previously for the effect of lithium on ELM stability.⁶ These plasmas share a similar shape, with major radius $R = 0.85$ m, minor radius $a = 0.6$ m (measured as the half-width at the midplane), elongation $\kappa \sim 2.0$, triangularity $\delta \sim 0.55$, as well as plasma current $I_p = 0.8$ MA, and toroidal magnetic field $B_t = 0.45$ T. The discharge without lithium coatings (the “pre-lithium” case) was heated with 4 MW of neutral beam injection (NBI). In the discharge with lithium coatings (“with-lithium”), the neutral beam heating was reduced to 2 MW, necessary in order to achieve the same stored energy in the two cases given the improved energy confinement observed in the with-lithium case (the power reduction was also necessary to avoid global stability limits with lithium). Figure 1 shows time traces of the plasma current, neutral beam power, plasma stored energy and electron

^{a)}Paper JI2 1, Bull. Am. Phys. Soc. 55, 148 (2010).

^{b)}Invited speaker.

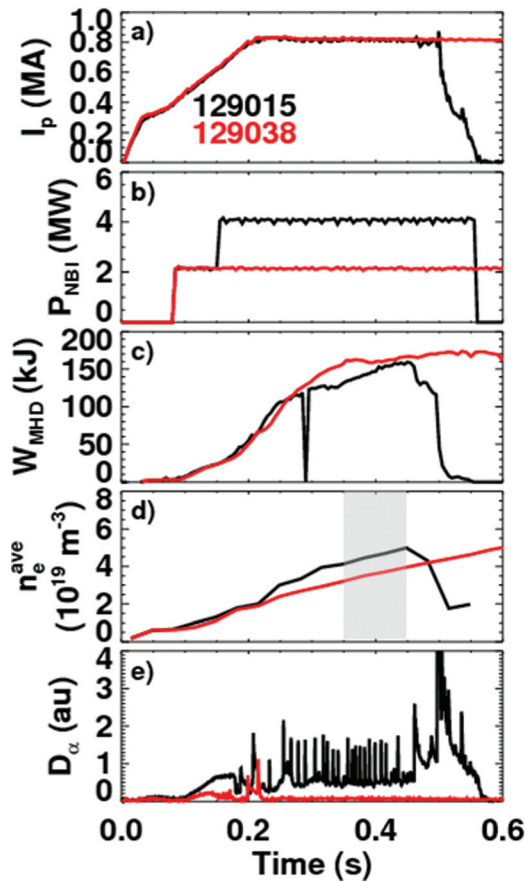


FIG. 1. (Color online) Time traces of a) plasma current, b) neutral beam input power, c) plasma stored energy, d) line-averaged electron density, and e) divertor D_α emission for pre- (black) and with-lithium (red/gray) discharges.

density, and divertor D_α emission during these two discharges. The shaded region in the density trace indicates the time window during which profile and fluctuation measurements were made (note that data from several discharges were combined to obtain the pre-lithium profiles, as only time slices from the last 20% of the ELM cycle were used).⁶

The pedestal profiles of electron density and temperature, ion temperature, and total pressure are shown in Figure 2 for both the pre- and with-lithium discharges. The electron density shows a very different shape in the with-lithium case compared to the pre-lithium discharge, with the density gradient in the pedestal reduced, but the radial extent of the steep-gradient region extended further into the plasma such that the density at the pedestal top is comparable in the two cases. The electron temperature, in contrast, is similar in the two cases for radii outside of $\psi_N \sim 0.95$. Inside this radius, the temperature gradient is much stronger in the with-lithium case, with the steep gradient characteristic of the pedestal extending farther into the plasma similar to the density profile. The ion temperature is also higher in the with-lithium case. However, in these and many other ELM-free discharges, the carbon 6+ density drops to low values near the plasma edge. This causes the charge-exchange data to become unreliable outside $\psi_N \sim 0.9$, where the gradient is presumably steepened in the with-lithium case. Hence, changes to ion heat transport at the edge cannot be addressed, and so this paper focuses on electron transport.

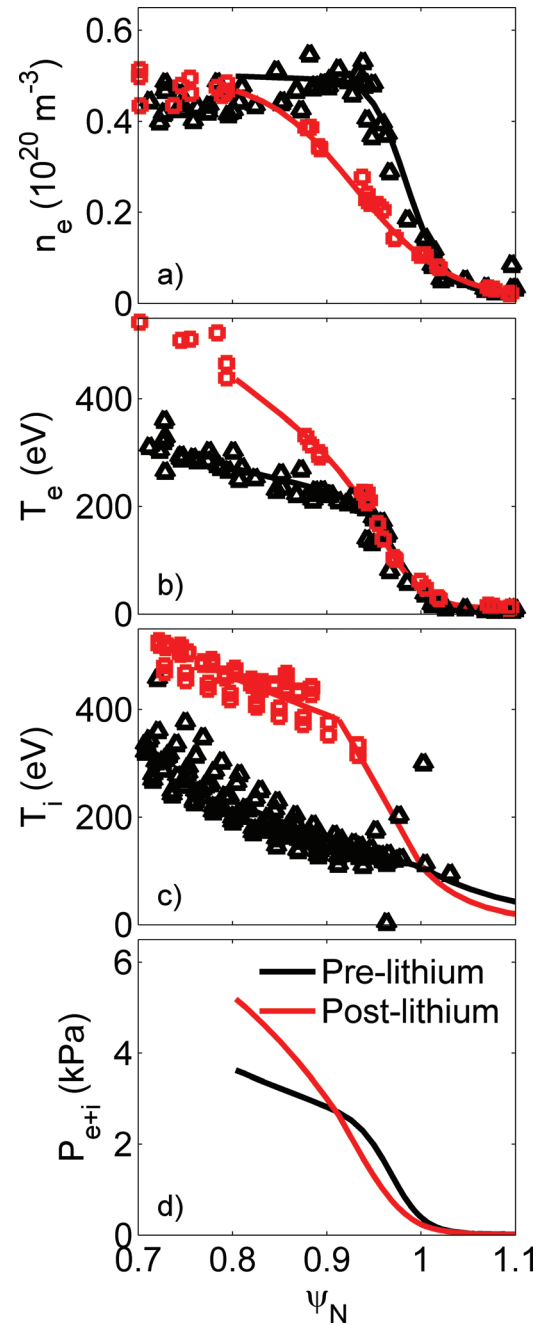


FIG. 2. (Color online) Edge profiles without (black) and with (red) lithium of a) electron density, b) electron temperature, c) ion temperature, and d) total pressure.

The net result of the modification to the density and temperature profiles is that the pressure pedestal is much wider with lithium coatings [panel 1(d)]: the electron pressure pedestal width increases from $\sim 5\%$ to $\sim 11\%$ in poloidal flux with lithium, or from 1.3 cm to 2.3 cm at the outer midplane. Outside of $\psi_N \sim 0.95$, the pressure gradient is reduced with lithium; this and the resulting reduction in bootstrap current aid in the stabilization of peeling-ballooning modes.⁶ With lithium, however, the wider pedestal region with strong pressure gradient more than compensates for this loss in far edge pressure gradient, giving an increased pressure at the pedestal top and a corresponding improvement in energy confinement.

In the remainder of this paper, interpretive modeling of these experiments will be presented. This modeling shows a widening of the transport barrier region in the electron heat and particle transport coefficients, with a marked decrease in transport in the range $\psi_N \sim 0.8-0.95$. Furthermore, a reduction in edge density fluctuation levels is also measured in the with-lithium discharge using multiple diagnostics. The interpretive modeling methods are described in Sec. II, and the results are given in Sec. III. Section IV presents measurements of turbulence made in discharges with varying lithium coatings. Possible mechanisms for the pedestal transport are discussed in Sec. V and conclusions are given in Sec. VI.

II. INTERPRETIVE MODELING USING THE SOLPS CODE

The edge transport properties of the pre- and with-lithium discharges have been analyzed using the SOLPS suite of codes,¹⁷ which solves a set of 2-D equations for the coupled plasma and neutral transport. The plasma is treated with a 2-D fluid approximation using the B2 code,¹⁸ with transport parallel to the magnetic field governed by classical Braginskii-type equations (with corrections for kinetic effects) and cross-field transport given by user-specified “anomalous” transport coefficients. Neutral transport is calculated by the EIRENE Monte Carlo code.¹⁹ The code has the ability to treat multiple impurity species; in the present work, pure deuterium simulations as well as runs with carbon included are performed (lithium is not considered as an impurity species, since the lithium concentration has been measured to be less than $\sim 0.1\%$ in other discharges with thick lithium coatings).⁸

SOLPS is used to interpretively model the discharges in the present work, giving the cross-field particle and energy transport coefficients that are required to reproduce measured profiles, while self-consistently including the contributions of neutrals and radiation. This is accomplished by adjusting the transport coefficients to give a match to fitted profiles of the upstream density and temperature profiles (the same fits have also been used in stability analysis).⁶ Here only diffusive transport is considered, whereas transport is likely to have convective components as well at the plasma edge;²⁰⁻²² the resulting transport coefficients can, therefore, be considered “effective” diffusivities for the purpose of comparing transport rates across discharges. This procedure using the SOLPS code has been benchmarked against other 1.5-D and 2-D interpretive transport codes [e.g., UEDGE (Ref. 23)] and has been found to give similar effective diffusivities.²²

In addition to the midplane measurements of the density and temperature profiles, measurements made using a calibrated D_α camera and an infrared thermography system are used to constrain the modeling. The D_α camera is used to constrain the particle recycling coefficient at the divertor plates—a free parameter in the modeling. This is adjusted so that the D_α emission from the simulation matches that measured in the experiment. The position of the separatrix with respect to the midplane profiles is constrained using the heat flux measurements: the profiles are shifted relative to the flux surfaces such that the simulated heat flux onto the divertor matches measurement (the magnitude of this shift is typically less than 1%

of the normalized poloidal flux). This effectively constrains the value of the separatrix electron temperature. The details of the methods used to achieve these reproductions of measurements in the code, as well as comparisons to the various diagnostics, can be found in Ref. 24. The results of the fitting method are illustrated in Figure 2, where the solid curves are the data from the SOLPS simulations.

III. TRANSPORT COMPARISON BETWEEN PRE- AND WITH-LITHIUM DISCHARGES

A. Analysis assuming pure deuterium plasmas

To evaluate the particle transport, a set of simulations were performed using pure deuterium in the calculations. In these runs, the input power was set to match the values from experiment (~ 4 MW for the pre-lithium case and ~ 2 MW with lithium). Similarly, the beam particle inputs were matched to the experimental values, as was a gas puff from the center column. To accurately account for the contribution of recycled neutrals to particle fueling, the divertor D_α emission was matched to the experimental value by adjusting the PFC recycling coefficient used in the simulations, as described in Sec. II. This method indicates a reduction in recycling coefficient R_{div} from ~ 0.98 without lithium to $R_{\text{div}} \sim 0.9$ with-lithium;²⁴ this recycling reduction is expected due to the pumping of D+ by the lithium. Due to the reduced recycling levels, the total source in the pedestal region is reduced by 50% in the with-lithium case compared to pre-lithium.

With only deuterium included in the simulation, the deuterium density is forced to equal the electron density in order to maintain quasi-neutrality. In experiment, on the other hand, the edge can have strong contributions from impurity species (see Sec. III B). The deuterium sources are accurately calculated by this method, and assuming that deuterium is the dominant electron source in the plasma core, this yields an effective electron particle diffusivity D_e^{eff} . This can be considered as representative of the total particle transport, without the need to consider the detailed transport properties of individual ion species. The same simulations yield the effective electron thermal diffusivity, although they are lacking the contribution of impurity radiation to the electron energy balance. Further calculations described below including carbon show that this effect makes only a small contribution in the pedestal.

The profiles of D_e^{eff} and χ_e^{eff} from the D-only modeling are shown in Figure 3. In the pre-lithium case, these show a radial structure typical of H-mode edge transport coefficients,²⁵ with a relatively large value inside the pedestal, small values within the pedestal, and increasing to large diffusivities towards the separatrix into the SOL (the strong increase in D_e^{eff} with radius in the SOL may be indicative of outward particle convection, which is not captured in this diffusive model). Inside the steep gradient region ($\psi_N < 0.9$), the density profile becomes very flat, and the particle diffusivity becomes correspondingly large. Due to sensitivity to the very small density gradient in this region, the inferred D_e^{eff} has a large uncertainty and so the absolute value is not emphasized here; nonetheless the radial position at which D_e^{eff} becomes large serves as a measure of the end of the

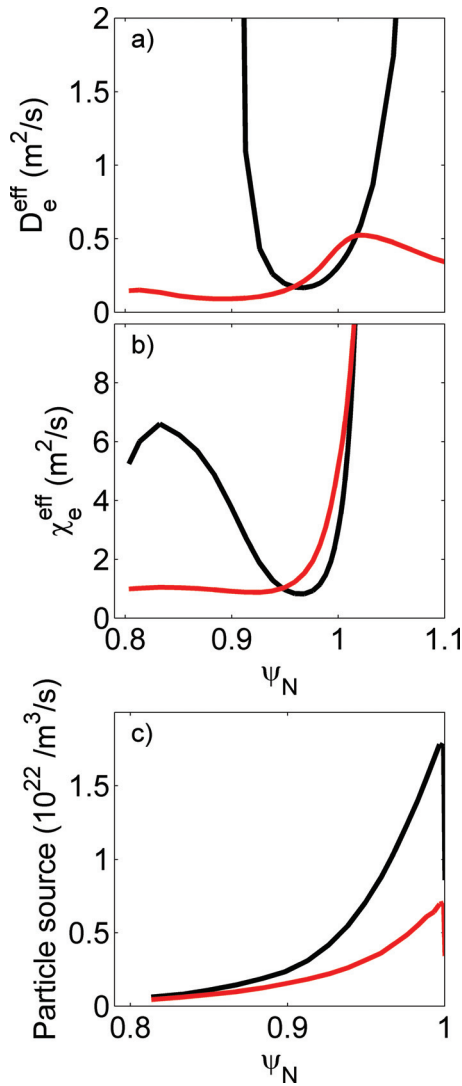


FIG. 3. (Color online) Effective diffusivities a) D_e^{eff} and (b) χ_e^{eff} , and c) total radial particle flux from pure deuterium modeling for pre- (black) and with-lithium (red/gray) discharges.

steep gradient region. In the with-lithium case, the changes to the transport coefficient are dependent on the radius. Towards the pedestal top, in the region $\psi_N \sim 0.8\text{--}0.95$, both the particle and thermal diffusivities are significantly reduced reflecting the steeper density and temperature gradients in this radial range. Near the separatrix, from $\psi_N = 0.95$ to 1, the transport coefficients are rather similar in the pre- and with-lithium cases; in fact, the with-lithium case shows somewhat increased transport in this region (although uncertainty in the separatrix position makes the precise comparison difficult).

Within the pedestal, the transport coefficients are similar between the two cases, with the minimum values in the with-lithium case comparable to those in the transport barrier region from the pre-lithium case. This is true for D_e^{eff} even though the density gradient is reduced in the with-lithium case, due to the reduced source and therefore radial particle flux caused by the lower recycling levels. The particle source rate averaged over the closed flux surfaces is shown in Figure 3; the lower source rate results in a 50% reduction of the radial particle flux in the with-lithium case. The same is

true for the radial heat flux, which is reduced by 50% in the with-lithium case due to the reduction of neutral beam input power. In terms of the effective diffusivities, the residual transport level in the pedestal is, therefore, similar in the pre- and with-lithium cases, and the main difference is the radial extent of the transport barrier, which is significantly wider with lithium.

B. Transport simulations including carbon

As described above, the deuterium-only cases give an estimate of the electron (and therefore total) particle transport. In order to estimate the transport properties of deuterium directly, as well as to account for the contribution of impurity radiation to electron power balance, additional simulations have been performed including carbon, which is the dominant impurity in these plasmas (lithium contamination is negligible⁸). As the carbon source is quite localized to the plasma edge and the radial carbon flux is nearly zero inside the separatrix, an inward convection is needed for the carbon species in order to account for the measured concentration. In the modeling, the same diffusivity is used for all ion species, and deuterium is again modeled by pure diffusion. An inward carbon pinch (the same value is used for all carbon charge states) is adjusted so that the simulated carbon density matches that measured using a charge exchange recombination spectroscopy system.

The measured and simulated total and carbon contribution to the electron density are shown in Figure 4, as well as the inferred deuterium density. For the pre-lithium case, the carbon contribution in the pedestal is relatively small, and the deuterium profile is similar in shape to the electron density profile. In the with-lithium case, however, carbon dominates the total electron density at the top of the pedestal, so that the pedestal in the deuterium density is somewhat narrower than that in the electron density (although still broader than the pre-lithium case). This is reflected in the effective deuterium diffusivity $D_{D^+}^{\text{eff}}$ —also shown in Figure 4, along with the electron particle diffusivity for the simulations with carbon—which shows a narrower barrier region than is seen for D_e^{eff} , but still with a widened barrier in the with-lithium case compared to pre-lithium. However, analysis of other discharges using the UEDGE (Ref. 23) code (with a transport model including convection and poloidally varying transport coefficients) has found an increase in D_{D^+} at all simulated radii with lithium,²⁶ suggesting that this decrease in the deuterium transport inside $\psi_N \sim 0.95$ may not be ubiquitous. The broadening of the electron density pedestal with lithium, on the other hand, is routinely observed; further analysis is required to document the changes in transport of the individual ion species across many discharges.

These simulations allow the contribution of carbon radiation to the electron power balance to be assessed. As shown in Figure 4, the profile of χ_e^{eff} required to match the measured T_e profile is similar to the results using deuterium alone in the simulation, both in shape and magnitude. This indicates that the radiation has a small effect on the edge electron heat transport properties, and that pure deuterium simulations are largely sufficient to yield an accurate χ_e^{eff} profile.

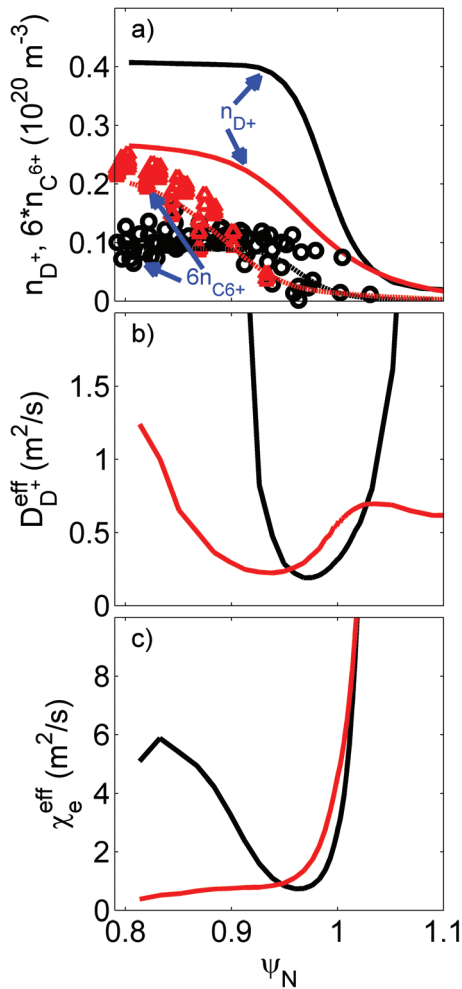


FIG. 4. (Color online) a) Measured contribution of carbon 6+ to electron density (circles), $n_{C^{6+}}$ from SOLPS modeling (dashed lines), and deuterium density (solid lines) from SOLPS; b) deuterium diffusivity D_{D+}^{eff} , and c) electron thermal diffusivity χ_e^{eff} from modeling including carbon of the pre- (black) and with-lithium (red/gray) discharges.

C. Discharges with intermediate lithium coating thickness

In addition to the cases studied so far (no lithium and sufficient lithium to entirely suppress ELMs), a set of discharges have been analyzed with intermediate thicknesses of lithium coatings. These discharges are ELMing, and are heated with 4 MW of NBI. The ELM frequency decreases as the lithium layer is increased,⁷ until the plasma is entirely ELM-free with very thick coating and reduced input power as described above. Further details on these discharges can be found in Ref. 27. As the lithium thickness increases, the pedestal density profile becomes wider, as shown in Figure 5. The electron temperature remains fairly constant in the region outside of $\psi_N \sim 0.95$. Inside this region, the temperature gradient increases with lithium thickness.

SOLPS analysis has been performed of the discharges in these series, assuming pure deuterium plasmas to yield the electron particle and thermal diffusivities. As shown in Figure 5, the width of the barrier region in the particle transport coefficient increases as the lithium layer is increased, reflecting the widening observed directly in the n_e profile. The χ_e^{eff} profile

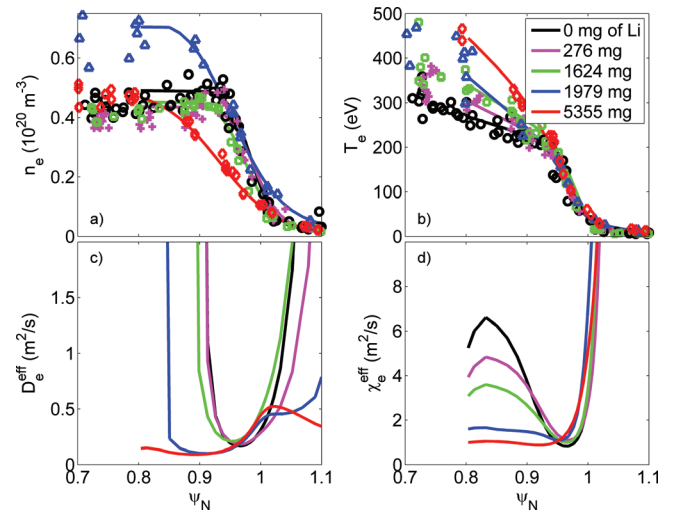


FIG. 5. (Color online) Profiles from scan of lithium thickness of a) electron density, b) electron temperature, c) D_e^{eff} and d) χ_e^{eff} .

does not show this widening, with the extent of the barrier region (where discernible) being relatively constant as the lithium thickness is changed. The larger effect is that χ_e^{eff} over the entire region $0.8 \leq \psi_N \leq 0.95$ gradually decreases with lithium, until in the final ELM-free case the low value of χ_e^{eff} obtained in the transport barrier extends all the way in to the inner boundary of the simulation. It is this radial extension of low values of χ_e^{eff} combined with the simultaneous widening of the n_e pedestal that yields the very wide pressure pedestal profile shown in Figure 2, which has been identified as the cause of the stabilization of ELMs with lithium.

D. Modifications to transport properties at the pedestal top and near the separatrix

Two regions can be identified in the profiles of the transport coefficients that show differing responses to the application of lithium to the PFCs. First, in the “pedestal top” region from $\psi_N \sim 0.8$ to 0.95 , the main difference between the pre- and with-lithium discharges is that the transport coefficients are greatly reduced with lithium. In the near-separatrix region, from $\psi_N \sim 0.95$ to 1.0 , the transport is not similarly reduced with lithium and, in fact, shows a somewhat higher value of the particle and thermal diffusivities. In this region, the T_e gradient is comparable in the pre- and with-lithium cases. Indeed, the T_e gradient is essentially unchanged throughout the intermediate-lithium cases (see Figure 5), which range over a variety of input powers, density, and density barrier width in addition to lithium thickness. The constancy of the T_e profile is suggestive of a critical gradient^{28,29} that determines the profile shape, in which case the effective diffusivities may not give a useful interpretation of the transport properties.

The stiffness of the T_e profile from $\psi \sim 0.95$ to 1.0 may be a crucial part of the ELM suppression observed with lithium coatings. When lithium is applied to the PFCs, the edge density is reduced. However, the electron temperature does not increase in response to this even for constant power, but remains fixed. As a result, the pressure gradient and hence

the bootstrap current are reduced near the separatrix, leading to the stabilization of peeling-ballooning modes.

IV. TURBULENCE MEASUREMENTS

A. Edge reflectometry

NSTX is equipped with reflectometers sensitive to electron density fluctuations in the pedestal region.³⁰ The system used in the studies presented here operates at five fixed frequencies (30, 35, 42, 44.5, and 50 GHz), with quadrature detection used to separate the phase and amplitude of the reflected signals. These reflectometer frequencies allow density fluctuations to be probed from approximately the pedestal top ($n_e^{\text{cutoff}} \sim 3.1 \times 10^{19}$ at 50 GHz) to near the separatrix ($n_e^{\text{cutoff}} \sim 1.1 \times 10^{19}$ at 30 GHz). An example of the raw signals measured is shown in Figure 6, where the in-phase and quadrature signals are shown in phasor form for the pre-lithium (panel a) and with-lithium (panel c) cases. The 50 GHz channel is shown, which has the innermost cutoff layer of the available channels. Due to the density profile changes, the position of this cutoff layer moves to lower major radius with lithium coatings, but in both the pre- and with-lithium cases, the layer is within the steep gradient region of the pedestal.

As is evident from these signals, the pre-lithium case shows very strong amplitude fluctuations in the reflected signals due to scattering near the cutoff surface, whereas in the with-lithium case, this effect is much smaller and fluctuations are mainly in the phase. This alone implies a change in the turbulence characteristics, although the change in density profile near the cutoff layer also needs to be accounted for as described below. A quantitative estimate can be made for the change in the RMS density fluctuation level $\delta n/n$ using some assumptions about the underlying turbulence and a synthetic diagnostic code.

For the with-lithium case, phase fluctuations can be related to the density fluctuations level via $\delta\phi \approx 2k_0L_n(\delta n/n)$ under the assumption that $k_r < L_n^{-1}$, where k_0 is the free space wavenumber and L_n is the density gradient scale length at the cutoff radius.³¹ These fluctuation levels as a function of the major radius are shown by the red curve in Fig. 8. To estimate $\delta n/n$ for the pre-lithium case, the Kirchhoff integral method described in Ref. 32 was used to simulate the reflectometer signal. In this physical optics calculation, which accounts for the 3-D geometry of the antennas and curvature of the cutoff surface, cutoff layer perturbations $\delta r \approx L_n(\delta n/n)$ are assigned a Gaussian spectral shape in k_θ

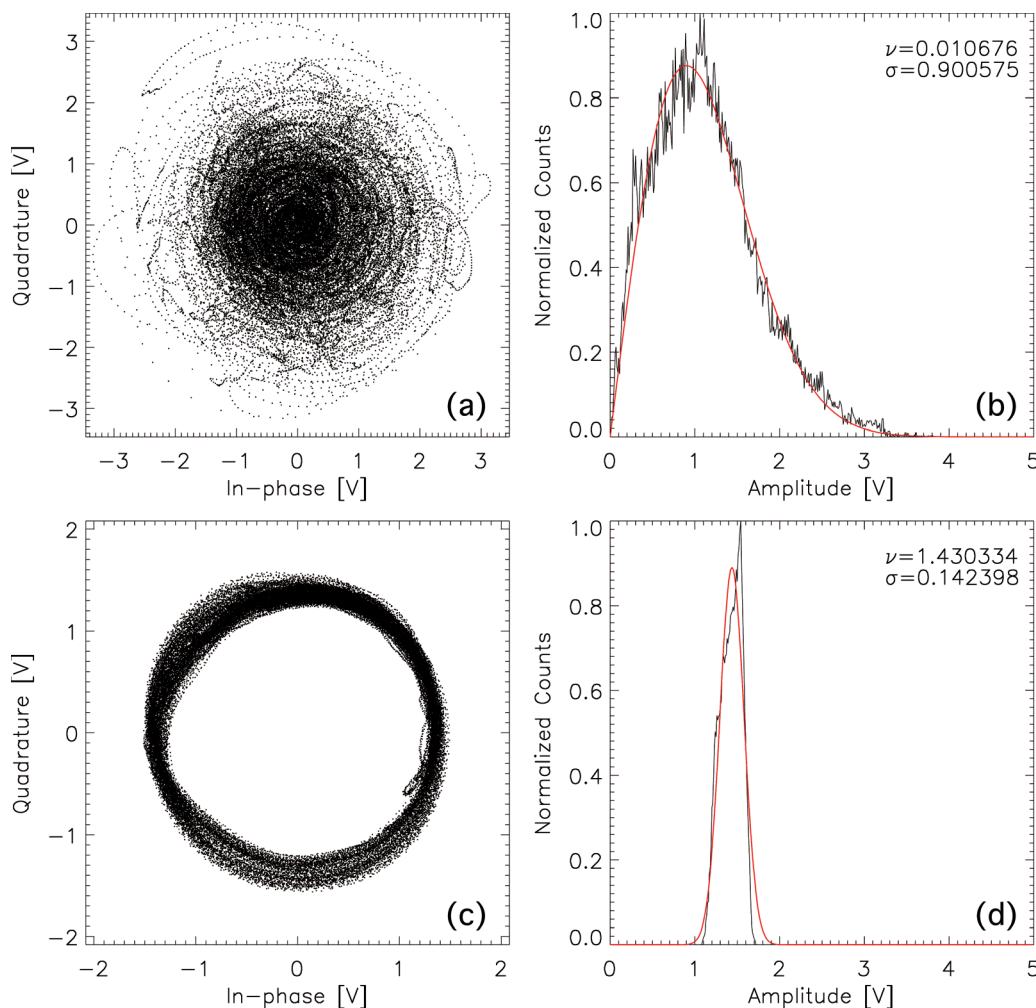


FIG. 6. (Color online) Reflectometer in-phase and quadrature signals for a) pre-lithium discharge (between ELMs) and c) with-lithium; measured amplitude PDF and fit to Rice distribution for b) pre- and d) with-lithium discharges.

$$|\delta n_{k_\theta}|^2 = \frac{8\sqrt{\pi}}{\Delta k_\theta} \left(\frac{\delta n}{n}\right)^2 e^{-k_\theta^2/\Delta k_\theta^2},$$

$$\delta n^{(s)}(x) = \sum_{k_\theta} |\delta n_{k_\theta}| \cos\left(\psi_{k_\theta}^{(s)} + 2\pi k_\theta x\right).$$

Here, the superscript (s) denotes the ensemble index, Δk_θ is the e-folding width, $\psi_{k_\theta}^{(s)}$ is a random phase term, and x is the spatial coordinate in the θ direction. At a given launch frequency, an ensemble of 30 000 data points (I and Q pairs) was generated for each set of values for the input parameter $\delta n/n$ and Δk_θ .

The ensembles of the simulated data as well as the time series of the experimental data can be characterized by the shape of the probability density function (PDF) of the signal amplitude $A = (I^2 + Q^2)^{1/2}$. The range of PDF shapes from a Rayleigh distribution (strong scattering) to a Gaussian distribution (weak scattering) can be approximated by the Rice distribution³³ for a signal containing a coherent sinusoidal component as well as Gaussian noise

$$P(A) = \frac{A}{\sigma^2} e^{-(A^2+v^2)/2\sigma^2} I_0\left(\frac{Av}{\sigma^2}\right),$$

where I_0 is the modified Bessel function of the first kind with zero order, and the shape of $P(A)$ is determined by the ratio of parameters v/σ . Here v is the amplitude of the coherent component, and σ is the amplitude of the Gaussian noise. Note that for small values of v/σ , $P(A)$ approaches the Rayleigh distribution [Fig. 6(b)], while for large values, $P(A)$ approaches a narrow offset Gaussian distribution [Fig. 6(d)].

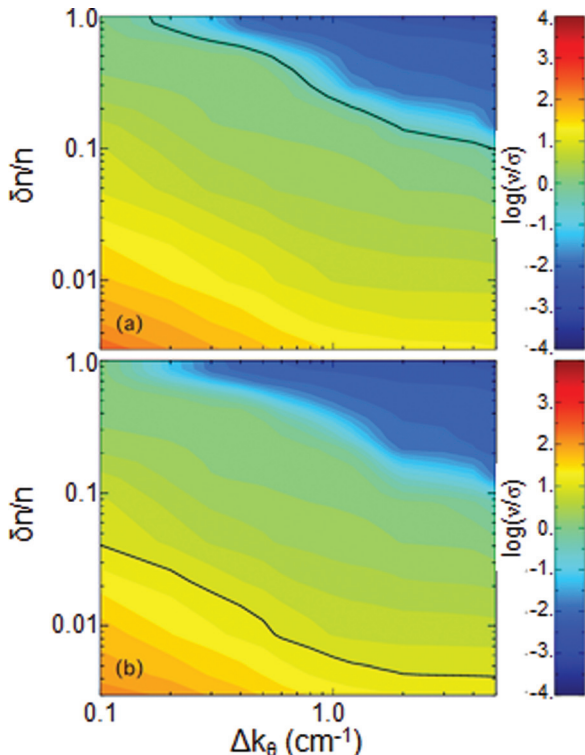


FIG. 7. (Color online) Simulated v/σ ratios for a) pre-lithium and b) with-lithium discharges. Solid black curves are experimental values.

Figure 7 shows the simulation results for the 50 GHz channel as color contours of v/σ for both the pre- and with-lithium cases. The solid black curves represent the contours for the experimental values of v/σ . In order to estimate $\delta n/n$ for the pre-lithium case, Δk_θ must be specified; here, we use Δk_θ determined from the with-lithium case as follows. In Fig. 7(b), the experimentally determined value of $\delta n/n \sim 0.006$ (see Fig. 8) intersects the experimental v/σ curve at $\Delta k_\theta \sim 1$ cm⁻¹. Similar values of Δk_θ are obtained from the other frequency channels as well. If we assume that the shape of the turbulence spectrum does not change between the two cases, then this value used with the experimental v/σ curve in Fig. 7(a) yields $\delta n/n \sim 0.24$.

The inferred profiles of $\delta n/n$ in the pre-lithium case are shown as the black curve in Fig. 8, as are the density and temperature profiles from the same time point as the reflectometer measurements. While this allows a comparison of the fluctuation level profiles between the pre- and with-lithium cases, it should be noted that the precise magnitude in the pre-lithium case remains somewhat uncertain given the assumptions required in making this estimate. For the pre-lithium case, the reflectometer measurement positions are at larger major radius relative to the pedestal than the with-lithium measurements, due to the change in the density profile shape. Nonetheless, the innermost pre-lithium measurements

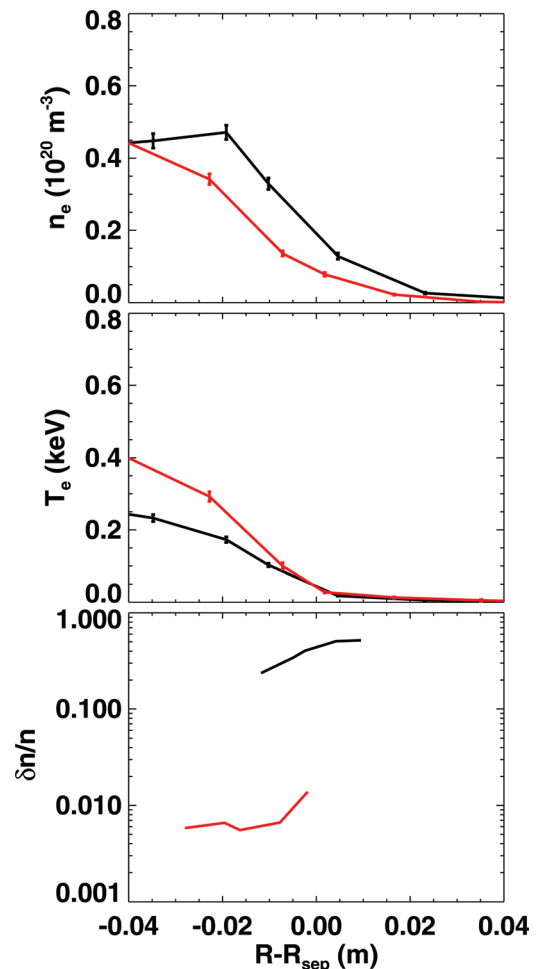


FIG. 8. (Color online) Profiles of a) n_e b) T_e and c) dn/n from reflectometer measurements in pre- (black) and with-lithium (red/gray) discharges.

are made in the inner part of the pedestal, near the top of the density pedestal, and these overlap with the outer channels for the with-lithium case.

In this region of overlap, a reduction of density fluctuations from on the order of 10% pre-lithium to $\sim 1\%$ with lithium is inferred. This reduction in fluctuations in the with-lithium case exists near the separatrix, which is contrary to the expectations based on the increased value of D_e^{eff} in this region. Further research is necessary to test if this near-separatrix turbulence reduction is persistent across many discharges.

B. High- k microwave scattering

NSTX is also equipped with a microwave scattering diagnostic capable of measuring the high-wavenumber portion of the turbulence spectrum,³⁴ which is expected to be important, e.g., electron temperature gradient (ETG) driven fluctuations.³⁵ In order to use this diagnostic to measure turbulence levels as lithium coatings are applied, a separate set of experiments was performed (this measurement was not available for the discharges analyzed above). The transition from little lithium to thick lithium coatings was repeated in a similar shape to that described above but with plasma current reduced to 650 kA. Time traces of several measurements from this lithium thickness scan are shown in Figure 9 and are qualitatively similar to those obtained in the discharges described above.

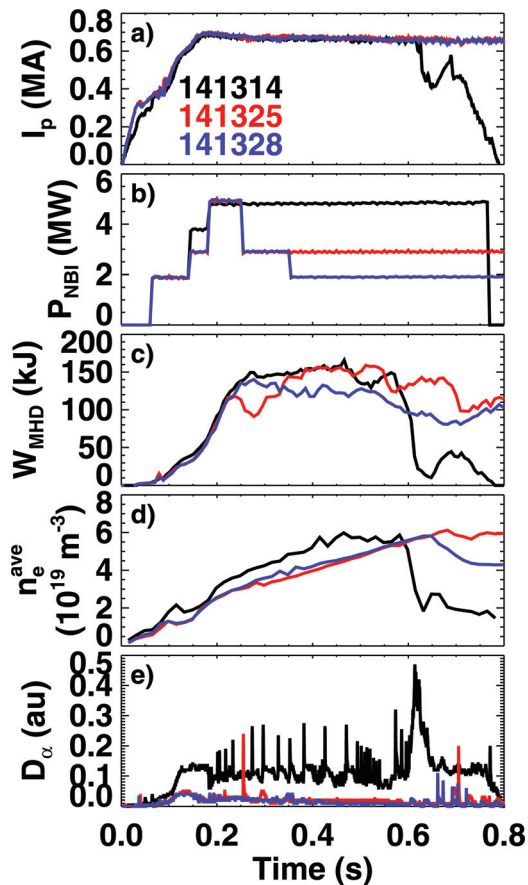


FIG. 9. (Color online) Time traces of a) plasma current, b) neutral beam input power, c) plasma stored energy, d) line-averaged electron density, and e) divertor D_α emission for a discharges with thin (black) and thick (red/light gray, blue/dark gray) lithium coatings.

The starting discharge for this scan did have a small amount of lithium applied to the PFCs between discharges. As can be seen in panel e, this was not sufficient to alter the presence of large ELMs, and so this case will again be referred to as “pre-lithium.” With thick lithium coatings, the plasma again becomes ELM-free with reduced divertor recycling, and the same stored energy is achieved even with the input power reduced (in this case from 5 MW to 3 MW). A further reduction to 2 MW with lithium is also shown, and in this case, the stored energy is somewhat lower than the pre-lithium case. As described below, the pedestal temperature profiles are similar in this low power case to the initial 5 MW pre-lithium case.

A similar modification to the pedestal structure as described in Sec. I was also obtained in the new experiments, as shown in Figure 10. As before, the input power was reduced to avoid global stability limits with lithium, from $P_{\text{NBI}} = 5$ MW in the pre-lithium case (black curves). With the power reduced to 3 MW with thick lithium coatings (red curves), a widening of the electron density pedestal was produced, as was an increase in the T_e gradient in the region $\psi_N \sim 0.8-0.9$ (T_e is again similar in the pre- and with-lithium cases from $\psi_N \sim 0.9$ to the separatrix). With P_{NBI} further reduced to 2 MW (blue curves), the density profile is again broadened from the pre-lithium case, but the increased T_e gradient is not observed. Rather, the edge temperature profiles in the 5 MW pre-lithium and 2 MW with-lithium cases are very similar.

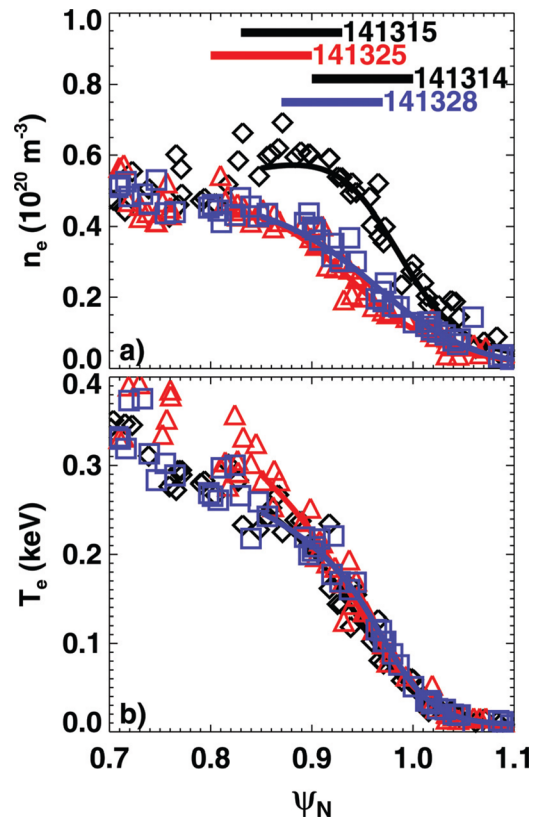


FIG. 10. (Color online) Pedestal a) density and b) temperature profiles from repeated experiment with little lithium at 5 MW (black), 3 MW thick lithium coatings (red/light gray) and 2 MW thick lithium coatings (blue/dark gray). Horizontal bars near shot labels indicate approximate scattering locations for each discharge.

The scattering locations of the high-k diagnostic for each of the cases are shown as the bars above the density profiles in Figure 10. Two bars are shown for the pre-lithium case, because multiple discharges were taken in which the high-k system was re-tuned to move the scattering location; the profiles shown use data combined from several time slices during these discharges. The system was tuned to measure near the pedestal top, where reduced transport is inferred; however, the spatial resolution of the system (~ 2 cm) is comparable to the width of the pedestal, and so the measurements cannot be entirely localized to this region of interest. The measured density fluctuation spectra are shown in Figure 11.

These measurements show the existence of high-k fluctuations in the edge region and allow the comparison between the various experimental conditions. As no absolute calibration is available for $\delta n/n$, the relative importance of these fluctuations in setting the total transport level cannot be assessed. Given the strong low-k fluctuations measured by reflectometry, it does appear likely that the high-k turbulence is not a dominant contributor in the pre-lithium case.

For the 3 MW with-lithium case, the scattering location was at the top of the pedestal (panel a), where strong differences exist in both the temperature and density gradients. Under these conditions, a reduction in density fluctuations by a factor of ~ 4 is measured at low k_{\perp} ($k_{\perp}\rho_s < 10$) in the 3 MW with-lithium case compared to pre-lithium (panel b). No reduction in fluctuations is observed at higher k_{\perp} ;

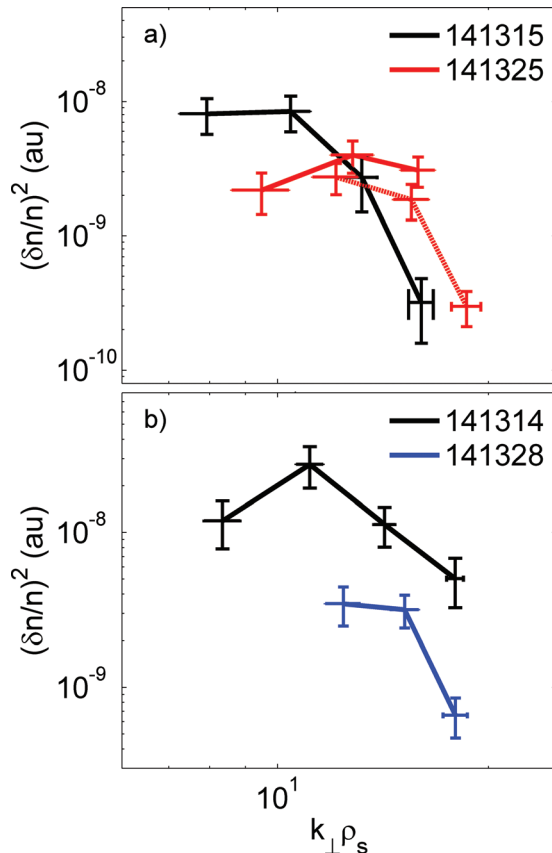


FIG. 11. (Color online) Density fluctuation spectra from high-k scattering diagnostic, comparing 5 MW ELMing discharges (black) with a) 3 MW (red/gray) and b) 2 MW (blue/gray) thick lithium coated ELM-free discharges.

instead, a shift of the spectrum to higher $k_{\perp}\rho_s$ is seen in the case with thick lithium coatings.

For the 2 MW with-lithium case, the scattering location was adjusted to measure at slightly larger radius (panel a). In this case, the pre-lithium discharge shows an increase in fluctuations at $k_{\perp}\rho_s > 10$ compared to the pre-lithium measurements made further inward (discharges 141314 and 141315 in Figure 9), with similar values at $k_{\perp}\rho_s < 10$. The 2 MW with-lithium case, on the other hand, shows similar fluctuation levels to those measured at the pedestal top at 3 MW with lithium. Compared to the 5 MW pre-lithium discharge measurements made in a comparable region of the pedestal (shot 141314), a strong reduction in fluctuation levels is observed in the 2 MW with-lithium case, with roughly a factor of five reduction measured across the power spectrum (panel c). This reduction is likely due to the significantly reduced power level. Note, however, that these two cases have similar temperature profiles even with these disparate power levels; with similar temperature gradients in the 5 MW pre-lithium and 2 MW with-lithium discharges, significantly less turbulence and radial heat flux are present with thick lithium coatings.

V. POSSIBLE MECHANISMS FOR TRANSPORT CHANGES WITH LITHIUM

A. ETG turbulence

While the interpretive modeling and fluctuation measurements described above indicate that transport and turbulence are significantly reduced with lithium near the pedestal top, the underlying mechanisms for this reduction are unclear. One candidate mechanism that can be considered is turbulence caused by ETG modes, as motivated by the measured reduction in short-wavelength turbulence using the high-k scattering system (although reflectometry also indicates a reduction at longer scales as well). ETG is chosen partially due to the expectation that long-wavelength turbulence is largely suppressed by shear in the radial electric field in the pedestal,³⁶ so that the short-wavelength fluctuations or the non-turbulent mechanisms are responsible for the residual transport levels. This is supported by the relatively small fluctuations measured by reflectometry in the with-lithium case, but the pre-lithium case is more likely dominated by the strong low-k fluctuations measured in the edge. Ion-scale turbulence could in principle also be examined; however, sensitivity to the electric field makes comparisons to experiment difficult given the uncertainty in this quantity. Furthermore, the gyrokinetic ordering is valid for electrons for these steep edge profiles ($\rho_e/L_{Te} < 1/400$ across the region examined) but may not be for ions.

The critical gradient for ETG mode onset is given approximately by

$$\left[\frac{R}{L_{Te}}\right] = \max\left(\eta_e^{\text{crit}} \frac{R}{L_n}, \left(1 + \frac{Z_{\text{eff}} T_e}{T_i}\right) \cdot (1.33 + 1.91 \hat{s}/q) \cdot F_G\right),$$

where R is the major radius, L_{Te} and L_n are the temperature and density gradient scale lengths, $\eta_e = L_n/L_{Te}$, \hat{s} is the magnetic shear, q is the safety factor, and F_G represents

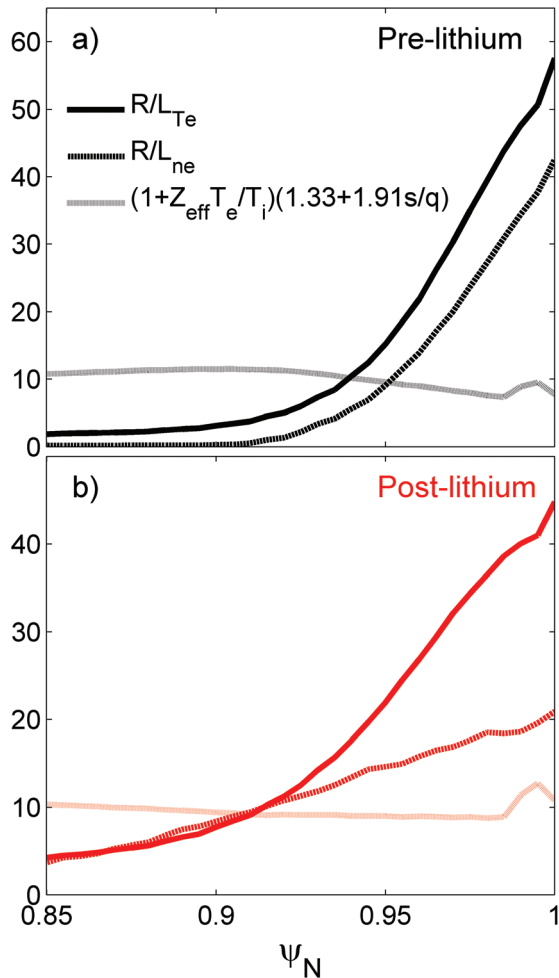


FIG. 12. (Color online) Profiles of normalized electron temperature (solid curves) and density (dashed) gradients, and ETG temperature ratio and shear factors (dotted) for a) pre-lithium and b) with-lithium cases.

additional variations due to the MHD equilibrium that are not easily quantifiable for spherical torus parameters.³⁷ The critical value η_e^{crit} is typically ~ 0.8 based on core ETG calculations, although calculations for the edge of ASDEX Upgrade plasmas have indicated a value of 1–1.25.³⁸ Figure 12 shows profiles of the normalized density and temperature gradients as well as the quantity $(1+Z_{\text{eff}}T_e/T_i)(1.33+1.91s/q)$ for the pre- and with-lithium cases. For both cases, the density gradient is strong outside of $\psi_N \sim 0.95$, so that the ETG threshold can be expected to be set by the density gradient. The measured electron temperature gradient scale lengths in this region, suggesting that ETG may play a role in the fairly stiff T_e profiles observed near the separatrix. Near the pedestal top, the density gradients are weaker in both the pre- and with-lithium cases, making the critical temperature gradient more sensitive to Z_{eff} , T_e/T_i , and the q -profile.

Based on this simple analysis, it does appear that ETG may be a contributor to the total transport at least in the with-lithium case, where only small low- k fluctuations are measured. In the future, more precise gyrokinetic calculations of the critical gradient as well as the nonlinear transport rates that can be expected from ETG modes will be performed.

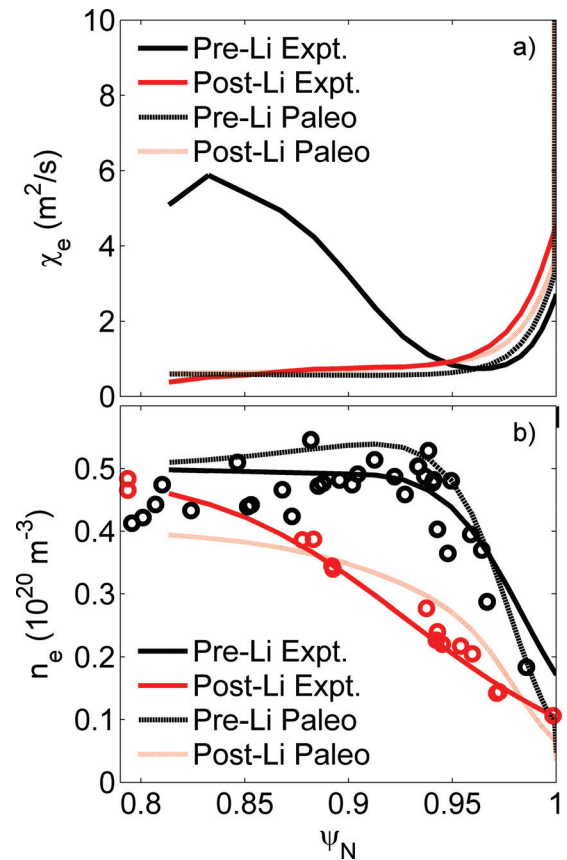


FIG. 13. (Color online) Experimental and paleoclassical values of a) χ_e^{eff} and b) density profile for pre- (black) and with-lithium (red/gray) discharges.

B. Paleoclassical transport

Another possible mechanism for setting the edge transport rates is paleoclassical transport, which is driven by the diffusion of poloidal magnetic flux.^{39,40} Paleoclassical transport depends strongly on the neoclassical resistivity and so is sensitive to the electron temperature and Z_{eff} profiles. Recently, a model of the pedestal structure based on paleoclassical transport within the pedestal and ETG at the pedestal top has been proposed and predictions have been made for the electron heat and particle transport.⁴¹

Profiles of χ_e from paleoclassical model are shown in Figure 13, along with the values from experiments, for the pre- and with-lithium cases (the resistivity profiles are obtained using the Z_{eff} data from the SOLPS calculations with carbon included as described above). In the near separatrix region, the paleoclassical predictions capture much of the structure seen in experiment, with χ_e being similar in magnitude and increasing with radius as ψ_N approaches 1.0. Furthermore, the paleoclassical values of χ_e also show the modest increase in the with-lithium case compared to pre-lithium observed near the separatrix. In the pedestal-top region, the experimental χ_e is significantly higher than the paleoclassical value for the pre-lithium case, suggesting that another transport mechanism dominates; in the with-lithium case, the agreement with paleoclassical remains good across the edge region.

The paleoclassical χ_e prediction⁴¹ is proportional to the magnetic field diffusivity D_η induced by the parallel neoclassical resistivity. The neoclassical resistivity contains

contributions from both the classical (Spitzer) resistivity (which depends on $Z_{\text{eff}}/T_e^{3/2}$) and parallel electron viscosity effects (which depend primarily on collisionality).⁴¹ In the steep gradient region ($0.94 < \psi_N < 1.0$), the density is reduced by a factor of ~ 2 in the with-lithium case. This reduces the collisionality and increases the viscosity effects by similar factors, and thereby increases the neoclassical resistivity (and χ_e) by $\sim 40\%$, as indicated in Figure 13. For $\psi_N < 0.9$, the competing effects of larger Z_{eff} but higher T_e with lithium largely cancel and cause the pre- and with-lithium cases to have similar neoclassical resistivity, and hence χ_e magnitudes as seen in Figure 13.

The density profile can also be predicted using the paleoclassical model (a strong inward particle pinch is predicted that nearly balances outward diffusion, so it is more straightforward to compare the density profile directly rather than diffusivities). Figure 13 shows the measured and paleoclassical edge density profiles. The paleoclassical density profile is scaled so that the average edge density from the model matches the magnitude of the experimental data; the paleoclassical model predicts the profile shape only and not the magnitude. The paleoclassical model again captures the experimental trends going from pre-lithium to with-lithium, with the density pedestal widening in the with-lithium case with a reduced gradient within the pedestal. In this application of the paleoclassical model, the density profile shape is determined by the resistivity profile only; the particle source due to neutrals is neglected, because this is expected to play a small role in the model. Note that in the paleoclassical model turbulence does not contribute a substantial fraction of the total transport inside the pedestal; under this model, changes in fluctuations would reflect changes to the profiles driving the microturbulence, but would not directly be an indicator of transport.

VI. DISCUSSION AND CONCLUSIONS

The work presented here has shown a significant reduction in the edge transport in discharges with thick lithium coatings on the PFCs in NSTX H-mode discharges, as analyzed using 2-D interpretive transport modeling. More precisely, a widening of the region with low transport coefficients is observed with lithium, with a significantly broader electron density pedestal. The electron heat transport is also reduced in the range $\psi_N \sim 0.8-0.95$, while the electron temperature profile appears to be stiff from $\psi_N \sim 0.95$ to the separatrix. At the same time, a significant reduction in edge turbulence has been measured in the discharges with heavy lithium conditioning. To some extent this is to be expected, because the change in edge profiles is likely to lead to changes in the turbulence. Hence, a causal relation between the reduced turbulence and transport changes cannot be presumed.

While the underlying causes for the change in transport with lithium are uncertain, two possible candidates have been identified that might be important for setting the residual transport in the pedestal. ETG turbulence may play a role in the near separatrix region, where a stiff T_e profile suggests that critical gradient physics might be important. Detailed, nonlinear calculations of ETG transport are required to explore this possibility further. Initial comparisons to a pale-

oclassical model of pedestal structure have also been performed and many features of the pre- to with-lithium comparison reproduced.

These results suggest that lithium, and wall conditioning and pumping techniques in general, may be a strong lever in controlling the properties of the H-mode pedestal. In the NSTX case, the change in structure leads to the elimination of ELMs, as well as improved global energy confinement. While further experiments are needed to optimize and explore the potential of lithiated PFCs to provide this control, further physics understanding is also required in order to make confident predictions for future devices. In particular, understanding the different responses to lithium coatings seen near the separatrix and at the pedestal top is necessary in order to optimize each region for good stability properties and for improving global energy confinement. Future research will focus on expanding this understanding, with the candidate transport mechanisms identified in this work serving as a starting point for these physics studies.

ACKNOWLEDGMENTS

This research was supported by the U.S. Department of Energy, Contracts DE-AC05-00OR22725, DE-FG02-99ER54527, DE-AC02-09CH11466, DE-FG02-92ER54139 DE-FC02-04ER54698, and DE-AC52-07NA27344.

¹A. E. Hubbard, *Plasma Phys. Controlled Fusion* **42**, A15 (2000).

²F. Wagner, G. Fussmann, T. Grave, M. Keilhacker, M. Kornherr, K. Lackner, K. McCormick, E. R. Müller, A. Stäbler, G. Becker, K. Bernhardt, U. Ditte, A. Eberhagen, O. Gehre, J. Gerhardt, G. v. Gierke, E. Glock, O. Gruber, G. Haas, M. Hesse, G. Janeschitz, F. Karger, S. Kissel, O. Klüber, G. Lisitano, H. M. Mayer, D. Meisel, V. Mertens, H. Murmann, W. Poschenrieder, H. Rapp, H. Röhr, F. Ryter, F. Schneider, G. Siller, P. Smeulders, F. Söldner, E. Speth, K.-H. Steuer, Z. Szymanski, and O. Vollmer, *Phys. Rev. Lett.* **53**, 1453 (1984).

³P. B. Snyder, H. R. Wilson, T. H. Osborne, and A. W. Leonard, *Plasma Phys. Controlled Fusion* **46**, A131 (2004).

⁴G. Federici, P. Andrew, P. Barabaschi, J. Brooks, R. Doerner, A. Geier, A. Herrmann, G. Janeschitz, K. Krieger, A. Kukushkin, A. Loarte, R. Neu, G. Saibene, M. Shimada, G. Strohmayer, and M. Sugihara, *J. Nucl. Mater.* **313-316**, 11 (2003).

⁵H. W. Kugel, M. G. Bell, J.-W. Ahn, J. P. Allain, R. Bell, J. Boedo, C. Bush, D. Gates, T. Gray, S. Kaye, R. Kaita, B. LeBlanc, R. Maingi, R. Majeski, D. Mansfield, J. Menard, D. Mueller, M. Ono, S. Paul, R. Raman, A. L. Roquemore, P. W. Ross, S. Sabbagh, H. Schneider, C. H. Skinner, V. Soukhanovskii, T. Stevenson, J. Timberlake, W. R. Wampler, L. Zakharov, *Phys. Plasmas* **18**, 056118 (2008).

⁶R. Maingi, T. H. Osborne, B. P. LeBlanc, R. E. Bell, J. Manickam, P. B. Snyder, J. E. Menard, D. K. Man, H. W. Kugel, R. Kaita, S. P. Gerhardt, S. A. Sabbagh, F. A. Kelly, and the NSTX Research Team, *Phys. Rev. Lett.* **103**, 075001 (2009).

⁷D. K. Mansfield, H. W. Kugel, R. Maingi, M. G. Bell, R. Bell, R. Kaita, J. Kallman, S. Kaye, B. LeBlanc, D. Mueller, S. Paul, R. Raman, L. Roquemore, S. Sabbagh, H. Schneider, C. H. Skinner, V. Soukhanovskii, J. Timberlake, J. Wilgen, and L. Zakharov, *J. Nucl. Mater.* **390-391**, 764 (2009).

⁸M. G. Bell, H. W. Kugel, R. Kaita, L. E. Zakharov, H. Schneider, B. P. LeBlanc, D. Mansfield, R. E. Bell, R. Maingi, S. Ding, S. M. Kaye, S. F. Paul, S. P. Gerhardt, J. M. Canik, J. C. Hosea, G. Taylor, and the NSTX Research Team, *Plasma Phys. Controlled Fusion* **51**, 124054 (2009).

⁹J. Winter, *Plasma Phys. Controlled Fusion* **38**, 1503 (1996).

¹⁰K. McCormick, M. Bessenrodt-Weberpals, E. R. Müller, J. Neuhauser, H. Niedermeyer, W. Poschenrieder, F. Ryter, U. Schneider, F. X. Söldner, K. H. Steuer, N. Tsois, O. Vollmer, and F. Wagner, *J. Nucl. Mater.* **176**, 89 (1990).

¹¹D. K. Mansfield, K. W. Hill, J. D. Strachan, M. G. Bell, S. D. Scott, R. Budny, E. S. Marmor, J. A. Snipes, J. L. Terry, S. Batha, R. E. Bell, M. Bitter, C. E. Bush, Z. Chang, D. S. Darrow, D. Ernst, E. Fredrickson, B. Grek, H. W. Herrmann, A. Janos, D. L. Jassby, F. C. Jobes, D. W. Johnson,

- L. C. Johnson, F. M. Levinton, D. R. Mikkelsen, D. Mueller, D. K. Owens, H. Park, A. T. Ramsey, A. L. Roquemore, C. H. Skinner, T. Stevenson, B. C. Stratton, E. Synakowski, G. Taylor, A. von Halle, S. von Goeler, K. L. Wong, S. J. Zweben, and the TFTR Group, *Phys. Plasmas* **3**, 1892 (1996).
- ¹²G. L. Jackson, T. S. Taylor, S. L. Allen, J. Ferron, G. Haas, D. Hill, M. A. Mahdavi, H. Nakamura, T. H. Osborne, P. I. Petersen, R. Seraydarian, M. Shimada, E. J. Strait, and P. L. Taylor, *J. Nucl. Mater.* **162**, 489 (1989).
- ¹³L. Peng, E. Wang, N. Zhang, D. Yan, M. Wang, Z. Wang, B. Deng, K. Li, J. Luo, and L. Liu, *Nucl. Fusion* **38**, 1137 (1998).
- ¹⁴J. D. Strachan, M. Bitter, A. T. Ramsey, M. C. Zarnstorff, V. Arunasalam, M. G. Bell, N. L. Bretz, R. Budny, C. E. Bush, S. L. Davis, H. F. Dylla, P. C. Efthimion, R. J. Fonck, E. Fredrickson, H. P. Furth, R. J. Goldston, L. R. Grisham, B. Grek, R. J. Hawryluk, W. W. Heidbrink, H. W. Hendel, K. W. Hill, H. Hsuan, K. P. Jaehnig, D. L. Jassby, F. Jobses, D. W. Johnson, L. C. Johnson, R. Kaita, J. Kampersroer, R. J. Knize, T. Kozub, B. LeBlanc, F. Levinton, P. H. La Marche, D. M. Manos, D. K. Mansfield, K. McGuire, D. H. McNeill, D. M. Meade, S. S. Medley, W. Morris, D. Mueller, E. B. Nieschmidt, D. K. Owens, H. Park, J. Schivell, G. Schilling, G. L. Schmidt, S. D. Scott, S. Sesnic, J. C. Sennis, F. J. Stauffer, B. C. Stratton, G. D. Tait, G. Taylor, H. H. Towner, M. Ulrickson, S. von Goeler, R. Wieland, M. D. Williams, K.-L. Wong, S. Yoshikawa, K. M. Young, and S. J. Zweben, *Phys. Rev. Lett.* **58**, 1004 (1987).
- ¹⁵G. L. Jackson, J. Winter, T. S. Taylor, K. H. Burrell, J. C. DeBoo, C. M. Greenfield, R. J. Groebner, T. Hodapp, K. Holtrop, E. A. Lazarus, L. L. Lao, S. I. Lippmann, T. H. Osborne, T. W. Petrie, J. Phillips, R. James, D. P. Schissel, E. J. Strait, A. D. Turnbull, and W. P. West, *Phys. Rev. Lett.* **67**, 3098 (1991).
- ¹⁶D. R. Ernst, B. Coppi, S. D. Scott, M. Porkolab, and TFTR Group, *Phys. Rev. Lett.* **81**, 2454 (1998).
- ¹⁷R. Schneider, X. Bonnin, K. Borrass, D. P. Coster, H. Kastelewicz, D. Reiter, V. A. Rozhansky, and B. J. Braams, *Contrib. Plasma Phys.* **46**, 3 (2006).
- ¹⁸B. J. Braams, *Contrib. Plasma Phys.* **36**, 276 (1996).
- ¹⁹D. Reiter, M. Baelmans, and P. Börner, *Fusion Sci. Technol.* **47**, 172 (2005), www.eirene.de.
- ²⁰S. I. Krasheninnikov, *Phys. Lett. A* **283**, 368 (2001).
- ²¹W. M. Stacey and R. J. Groebner, *Phys. Plasmas* **16**, 102504 (2009).
- ²²J. D. Callen, R. J. Groebner, T. H. Osborne, J. M. Canik, L. W. Owen, A. Y. Pankin, T. Rafiq, T. D. Rognlien, and W. M. Stacey, *Nucl. Fusion* **50**, 064004 (2010).
- ²³T. D. Rognlien, D. D. Ryutov, N. Mattor, and G. D. Porter, *Phys. Plasmas* **6**, 1851 (1999).
- ²⁴J. M. Canik, R. Maingi, V. A. Soukhanovskii, R. E. Bell, H. W. Kugel, B. P. LeBlanc, and T. H. Osborne, "Measurements and 2-D modeling of recycling and edge transport in discharges with lithium-coated PFCs in NSTX," *J. Nucl. Mater.* (in press).
- ²⁵A. V. Chankin, D. P. Coster, R. Dux, Ch. Fuchs, G. Haas, A. Herrmann, L. D. Horton, A. Kallenbach, M. Kaufmann, Ch. Konz, K. Lackner, C. Maggi, H. W. Muller, J. Neuhauser, R. Pugno, M. Reich, and W. Schneider, *Plasma Phys. Controlled Fusion* **48**, 839 (2006).
- ²⁶A. Yu. Pigarov, *Phys. Plasmas* (submitted).
- ²⁷R. Maingi, D. Boyle, J. M. Canik, J. Manickam, T. H. Osborne, P. B. Snyder, R. E. Bell, S. P. Gerhardt, R. Kaita, H. W. Kugel, B. P. LeBlanc, D. K. Mansfield, S. A. Sabbagh, and the NSTX Team, IAEA Fusion Energy Conference, Daejeon, Korea, 11–16 October 2010, Paper EX/D2-2.
- ²⁸A. M. Dimits, G. Bateman, M. A. Beer, B. I. Cohen, W. Dorland, G. W. Hammett, C. Kim, J. E. Kinsey, M. Kotschenreuther, A. H. Kritiz, L. L. Lao, J. Mandrekas, W. M. Nevins, S. E. Parker, A. J. Redd, D. E. Shumaker, R. Sydora, and J. Weiland, *Phys. Plasmas* **7**, 969 (2000).
- ²⁹B. LaBombard, J. W. Hughes, N. Smick, A. Graf, K. Marr, R. McDermott, M. Reinke, M. Greenwald, B. Lipschultz, J. L. Terry, D. G. Whyte, and S. J. Zweben, *Phys. Plasmas* **15**, 056106 (2008).
- ³⁰S. Kubota, W. A. Peebles, N. A. Crocker, R. Maingi, C. E. Bush, R. J. Maqueda, S. J. Zweben, R. E. Bell, B. P. LeBlanc, T. S. Hahn, and G. J. Kramer, *Bull. Am. Phys. Soc.* **53**, 188 (2008).
- ³¹R. Nazikian, G. J. Kramer, and E. Valeo, *Phys. Plasmas* **8**, 1840 (2001).
- ³²A. Ejiri, T. Yamada, Y. Adachi, O. Watanabe, and Y. Takase, *Plasma Phys. Controlled Fusion* **50**, 065003 (2008).
- ³³N. Levanon, *Radar Principles* (Wiley, New York, 1988), Chap.3, p. 42.
- ³⁴D. R. Smith, E. Mazzucato, W. Lee, H. K. Park, C. W. Domier, and N. C. Luhmann, *Rev. Sci. Instrum.* **79**, 123501 (2008).
- ³⁵W. Dorland, F. Jenko, M. Kotchenreuther, and B. N. Rogers, *Phys. Rev. Lett.* **85**, 5579 (2000).
- ³⁶K. H. Burrell, *Phys. Plasmas* **4**, 1499 (1997).
- ³⁷F. Jenko, W. Dorland, and G. W. Hammett, *Phys. Plasmas* **8**, 4096 (2001).
- ³⁸F. Jenko, D. Told, P. Xanthopoulos, F. Merz, and L. D. Horton, *Phys. Plasmas* **16**, 055901 (2009).
- ³⁹J. D. Callen, *Phys. Rev. Lett.* **94**, 055002 (2005).
- ⁴⁰J. D. Callen, C. C. Hegna, and A. J. Cole, *Phys. Plasmas* **17**, 056113 (2010).
- ⁴¹J. D. Callen, "A model of pedestal structure," UW-CPTC 10-6, August 30, 2010 (available at <http://www.cptc.wisc.edu>).